Journal of Alloys and Compounds 511 (2012) 251–256

Contents lists available at SciVerse ScienceDirect

Journal of Alloys and Compounds

journal homepage: www.elsevier.com/locate/jallcom

One-pot hydrothermal synthesis of ruthenium oxide nanodots on reduced graphene oxide sheets for supercapacitors

Yao Chen[a,b], Xiong Zhang[a], Dacheng Zhang[a,b], Yanwei Ma[a,*]

[a] Institute of Electrical Engineering, Chinese Academy of Sciences, Beijing 100190, PR China
[b] Graduate University of Chinese Academy Sciences, Beijing 100049, PR China

ARTICLE INFO

Article history:
Received 12 July 2011
Received in revised form
15 September 2011
Accepted 15 September 2011
Available online 19 September 2011

Keywords:
Energy storage materials
Chemical synthesis
Transmission electron microscopy

ABSTRACT

Ruthenium oxide nanodots have been deposited on reduced graphene oxide (RGO) sheets homogeneously by hydrothermal and annealing methods. Adding NaOH solution in GO colloids prevents the restack and agglomeration of GO sheets when mixed with ruthenium chloride solution. Local crystallization of RuO_2 in the composites is revealed by X-ray diffraction and transmission electron microscopy. The element mapping image demonstrates the uniform distribution of Ru on RGO sheets. Unlike the pure crystalline RuO_2 exhibiting poor electrochemical performance, the composites present superior capacitive properties. The hydrothermal time is optimized and a maximum of 471 $F g^{-1}$ is measured in the composites at 0.5 $A g^{-1}$ when loaded with 45 wt% of RuO_2. After 3000 cycles, its specific capacitance remains 92% of the maximum capacitance. Our results suggest potential application of the reduced graphene oxide/ruthenium oxide composites to supercapacitors.

1. Introduction

With higher power density than lithium ion batteries [1,2], supercapacitors have attracted great interest in the field of energy storage devices. Supercapacitors are ideal for applications including electric vehicles, emergency doors, portable electronic devices and so on [3,4]. The electrochemical energy storage mechanisms for supercapacitors encompass double electrical layer capacitance (separation of charges at the interface between a solid electrode and an electrolyte) and pseudocapacitance (fast faradaic reactions depending on multiple oxidation states of materials) [5]. Electrode materials based on the former mechanism are carbon materials and the latter are polymers and metal oxide [6].

Graphene is a 2D flat material consisting of monolayer carbon atoms [7]. Because of its high theoretical specific surface area and good electrical conductivity [8], graphene exhibits promising potential in energy storage applications [9–11]. Since Vivekchand et al. [12] and Stoller et al. [13] took the lead in fabricating graphene-based supercapacitors, the capacitive properties have been enhanced effectively by many researchers' unremitting efforts [14]. However, graphene based supercapacitors merely possess limited capacitance due to two main aspects. On one hand, solid graphene which is prone to restacking decreases its specific surface area severely. On the other hand, graphene as a carbon material is based on double electrical layer capacitance mechanism. Initially, in order to increase its specific surface area, some strategies to prevent graphene sheets from aggregating were studied by incorporating nanoparticles into graphene oxide [15–17]. Further, as we know, materials depending on pseudocapacitance mechanism have higher capacitive nature than carbon materials, but pure pseudocapacitance materials have poor life performance. For the sake of obtaining synergistic effects between the two mechanisms, graphene-based composites, such as graphene/polyaniline and graphene/Co_3O_4, are synthesized to be an alternative to bare graphene [9,18]. Up to now, hydrous ruthenium oxide nanodots exhibit the highest pseudocapacitance of 1580 $F g^{-1}$ and good electrical conductivity [19–21]. Subsequently, in the interest of effective inhibition of crystallite coalescence upon annealing, a series of hydrothermal studies were conducted by Chang et al. [22,23]. No doubt, ruthenium oxide nanodots can effectively improve the electrochemical properties of graphene after depositing on graphene sheets. Up to now, only one literature [24] reported hydrous ruthenium oxide anchoring on graphene by a direct sol–gel method for supercapacitors. However, it is difficult to re-disperse solid graphene in liquid phase with high quality. Conversely, homogeneous suspension can be obtained more convenient if using graphite oxide (GO) as the precursor instead of graphene.

Reduced graphene oxide (RGO) with a certain amount of oxygen can be obtained by a hydrothermal method [25]. The ruthenium oxide nanodots uniformly dispersed in the graphene oxide colloids is the precondition to settle ruthenium oxide on RGO sheets homogeneously. We have deposited ruthenium oxide nanodots homogeneously on RGO sheets by one-pot hydrothermal synthesis and then investigated the electrochemical properties of the

* Corresponding author. Tel.: +86 10 82547129; fax: +86 10 82547137.
E-mail address: ywma@mail.iee.ac.cn (Y. Ma).

0925-8388/$ – see front matter © 2011 Elsevier B.V. All rights reserved.
doi:10.1016/j.jallcom.2011.09.045

composites after annealing. When loading 45% of ruthenium oxide in the composites, a maximum capacitance of 471 F g^{-1} at the current density of 0.5 A g^{-1} has been obtained. The outstanding results are attributed to ruthenium oxide nanodots attached onto the surface of RGO sheets, facilitating the electron transfer from graphene to ruthenium oxide and hence building up with synergistic effects between double-layer capacitance and pseudocapacitance.

2. Experimental

2.1. Synthesis of composites

The preparation procedure of RGO/ruthenium oxide composites consists of sol–gel synthesis, followed with hydrothermal and annealing treatments with GO and hydrous ruthenium chloride as the precursors. Concretely, GO was prepared according to the modified Hummers' method [26]. 0.1 g of GO was sonicated in 80 mL of water for 2 h to form stable colloids. Next, 0.06 g of hydrous ruthenium chloride was dissolved in 12 mL of water. And then 0.4 M sodium hydroxide aqueous solution was injected into the GO colloids to adjust pH to 8. Afterwards, the alkaline colloids were added into the ruthenium chloride solution dropwise by a constant pressure funnel. Once mixed, 0.4 M sodium hydroxide solution was injected into to the mixture to adjust pH to 7. Subsequently, the neutral mixture was transferred to a stainless steel autoclave and heated at 180 °C for several hours. RGO/ruthenium oxide composites was obtained after filtration, washing with water, desiccation and annealing at 150 °C in air for 6 h. The samples before and after annealing were designated as GR-t and GRA-t, where t refers to hydrothermal time, respectively. For comparison, pure annealing ruthenium oxide and reduced graphene oxide whose hydrothermal time is 6 h were prepared as control experiments in a similar procedure.

2.2. Characterization

X-ray diffraction (XRD) analyses were performed using an X' Pert Pro system with Cu Kα radiation. X-ray photoelectron spectroscope (XPS) spectra were recorded on a PHI Quantear SXM (ULVAC-PH INC) which used Al as anode probe in 6.7×10^{-8} Pa. Raman spectra were obtained on a RM 2000 microscopic confocal Raman spectrometer (Renishaw in via Plus, England), employing a 514 nm laser beam. The thermogravimetric analysis (TGA) was carried out by TA Q600SDT. Surface area analysis was determined with Micromeritics TriStar II 3020. The sample was outgassed at 150 °C prior to analysis. A Hitachi S4800 field emission scan electron microscope (FESEM) with energy dispersive spectroscopy (EDS) was utilized for morphology observation and elemental mapping. The substrate of the FESEM/EDS specimens is a pure Al strip. Transmission electron microscopy (TEM) morphology was investigated by JEOL JSM 2010F. The electrical conductivities of bulk RGO after annealing and GRA-6 by pressing the powder at 5 MPa in room temperature were detected with a physical property measurement system (Quantum Design, PPMS).

2.3. Electrochemical measurements

All electrochemical properties were measured with 1 M H_2SO_4 as the electrolyte in a three-electrode configuration. The working electrode consisted of a titanium foil as a current collector and a mixture of active materials, acetylene black and polyvinylidene difluoride with a weight ratio of 8:1:1. A slice of platinum was used as the auxiliary electrode and a saturated calomel electrode (SCE) as the reference electrode. The cyclic voltammetry (CV) and galvanostatic charge/discharge were performed with CHI 660C workstation except the life test was operated with Arbin MITS PRO 4.27.

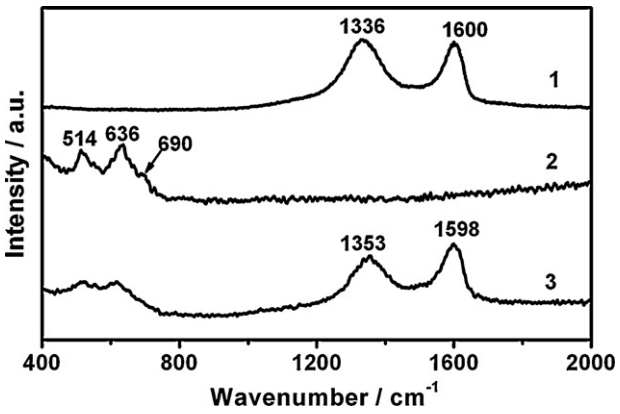

Fig. 2. Raman spectra of (1) RGO and (2) RuO_2 after annealing and (3) GRA-6.

3. Results and discussion

As GO colloids are not stable in an acid environment with low pH value, aggregation happens when acidic ruthenium chloride solution is mixed with GO colloids. Recently, a general strategy to fabricate graphene/metal oxide composites proposed a new route of adjusting pH before hydrothermal treatment [27]. Thus it is necessary to inject NaOH solution to the GO colloids so that a stable mixture of GO and ruthenium chloride is obtained. Further, the alkaline GO colloids should be added to the ruthenium chloride solution, otherwise sediment of ruthenium oxide could be formed before depositing on GO sheets. After the hydrothermal reaction, ruthenium oxide could be deposited on RGO sheets homogenously.

Fig. 1 features the structure of pure ruthenium oxide before and after annealing, GR-6 and GRA-6. The XRD patterns of ruthenium oxide before and after annealing show four peaks indexed in the figure, which correspond to rutile RuO_2. As for GR-6, no crystalline diffraction peaks of GO at $2\theta = 11°$, graphite at $2\theta = 26°$ and RuO_2 are observed, revealing that GO is reduced and amorphous RuO_2 nanodots as spacers are deposited on RGO sheets. After annealing, the broad peaks of RuO_2 emerge in GRA-6, but completely crystalline RuO_2 in the composites is still not formed. These results demonstrate that crystal growth of RuO_2 is restrained in the presence of RGO. In order to further characterize the phase structure of RGO and RuO_2 after annealing and GRA-6, the Raman spectra of them

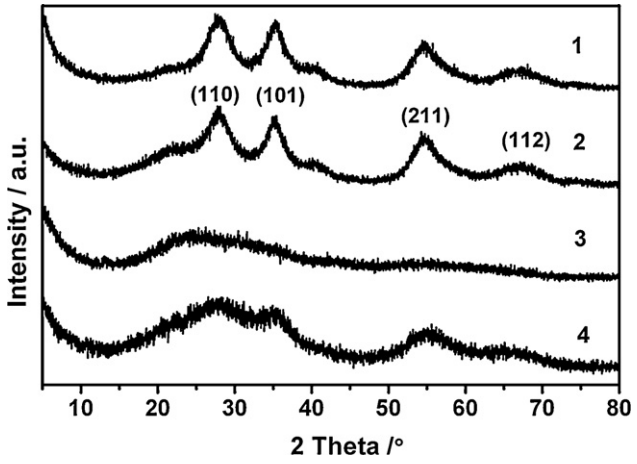

Fig. 1. XRD patterns of RuO_2 (1) before and (2) after annealing, (3) GR-6 and (4) GRA-6.

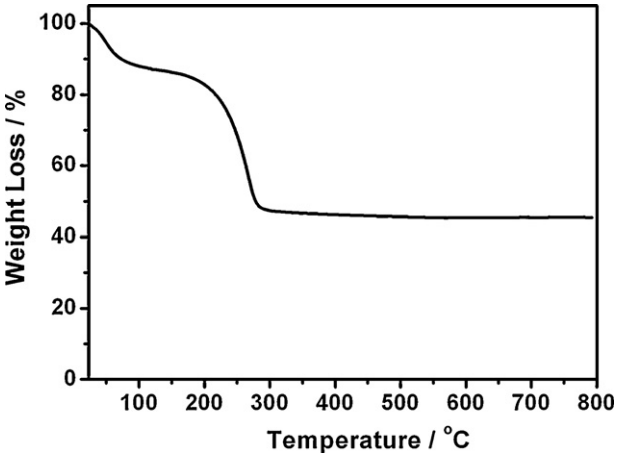

Fig. 3. TGA of GRA-6.

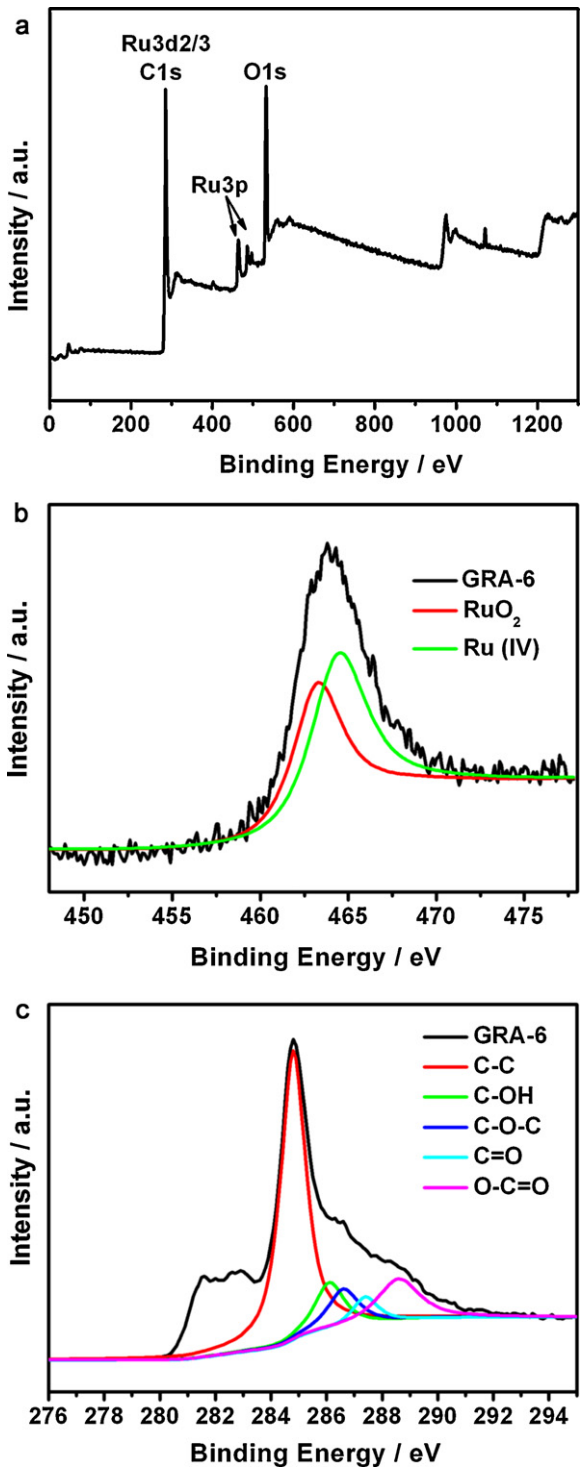

Fig. 4. The XPS (a) survey, (b) Ru3p 3/2 and (c) C 1s spectrum of GRA-6.

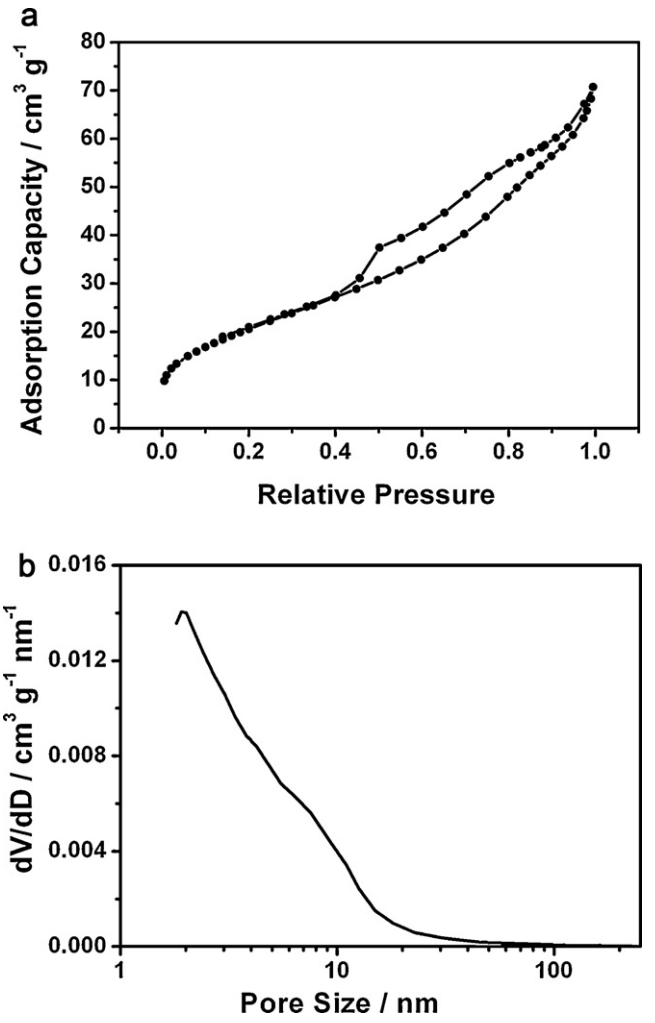

Fig. 5. (a) Nitrogen adsorption/desorption isotherm and (b) pore-size distribution of GRA-6.

are shown in Fig. 2. Like other graphene materials synthesized by chemical methods, RGO also shows its D and G bands. Three distinct peaks of 514, 636, 690 cm^{-1} are observed in RuO_2 after annealing. Besides these peaks, the D (1353 cm^{-1}) and G (1598 cm^{-1}) bands also are present in the composite, suggesting that the in situ integration of RGO and RuO_2 could be achieved by the method.

The TGA in Fig. 3 demonstrates that the content of RuO_2 in GRA-6 reaches 45%. The XPS survey spectrum (Fig. 4a) of GRA-6 exhibits Ru $3p_{1/2}$ and $_{3/2}$ at 486 and 464 eV in addition to C 1s and O 1s. Fig. 4b shows the fitting $Ru3p_{3/2}$ spectrum of GRA-6, where two peaks at 463.2 and 464.4 eV are assigned to RuO_2 [28] and Ru IV. It is confirmed that RuO_2 is formed in the hydrothermal course. The C 1s spectrum of GRA-6 overlaps its $Ru3d_{3/2}$. However, as shown in Fig. 4c, the spectrum of GRA-6 has only a main peak at 284.8 eV corresponding to C–C bond. Assuming that $Ru3d_{3/2}$ has no influence on the C 1s spectrum, the peak intensities of C–OH (286.1 eV) [29], C–O–C (286.6 eV), C=O (287.4 eV) and O–C=O (288.6 eV) in GRA-6 are very weak, in comparison with those in GO, indicative of reducing GO in the hydrothermal reaction.

As shown in Fig. 5a, the nitrogen adsorption and desorption isotherm of GRA-6 possesses a hysteresis loop and an inflection point in a relatively low pressure. It consists with a type IV isotherm, reflecting the presence of mesoporous characteristic in the sample. Its Brunauer–Emmett–Teller (BET) specific surface area reaches 76 $m^2\ g^{-1}$. Considering that the surface area of solid aggregated RGO cannot be detected in the same condition, the relatively large surface area of GRA-6, combining with absence of graphite peaks in its XRD pattern, proves that these RuO_2 nanodots keep RGO sheets individual by anchoring on them. Considering that pore size calculation from the desorption branch is affected by tensile strength effect [30], the pore size distribution curve of GRA-6 is obtained from adsorption branch by the Barret–Joyner–Helena (BJH) analyses. Fig. 5b shows broad size distribution below 11 nm with an average pore width of 6 nm. Withal, the BJH adsorption cumulative volume of pores between 1.7 and 300 nm width is up to 0.105 $cm^3\ g^{-1}$ for GRA-6.

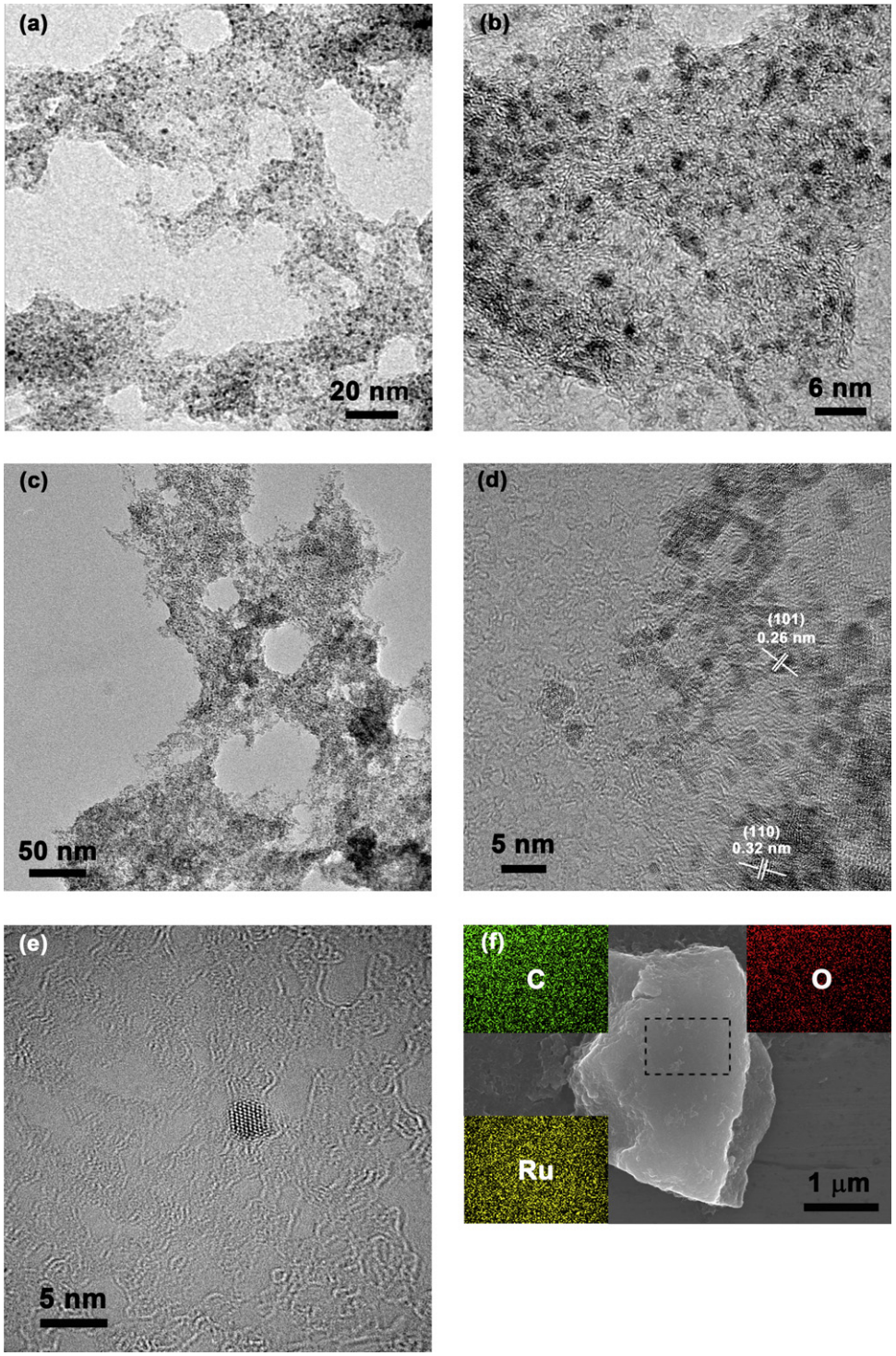

Fig. 6. Low magnification TEM images of (a) GR-6 and (c) GRA-6, high resolution TEM images of (b) GR-6, (d) GRA-6 and (e) RuO_2 after annealing and (f) SEM image of GRA-6 with element mapping images in its inset.

The morphology of GR-6 and GRA-6 are shown in Fig. 6. For GR-6, densely stacked RuO_2 nanodots are partly present in Fig. 6a due to agglomeration and corrugation of RGO sheets. In the high resolution TEM image (Fig. 6b), amorphous RuO_2 nanodots with 1.5 nm deposited on RGO sheets uniformly are observed before annealing. After annealing, the low magnification morphology of GRA-6 in Fig. 6c is similar to that of GR-6. By further observation in the high resolution TEM image, local crystalline RuO_2 nanodots are formed on RGO sheets with lattice fringes marked by arrows in Fig. 6d, which is in agreement with the two main broad peaks in the XRD results. However, their sizes are not changed obviously. As for the control experiment, the diameter of the annealing RuO_2 nanodot with a very clear lattice image is still below 3 nm, as revealed by Fig. 6e. Effective inhibition of crystallite coalescence and maintenance of nano-scale for RuO_2 nanodots, whether as a single ingredient or in the composites, depend on the hydrothermal process used before annealing [22,31]. During the initial period of hydrothermal process, the two precursors are co-precipitated

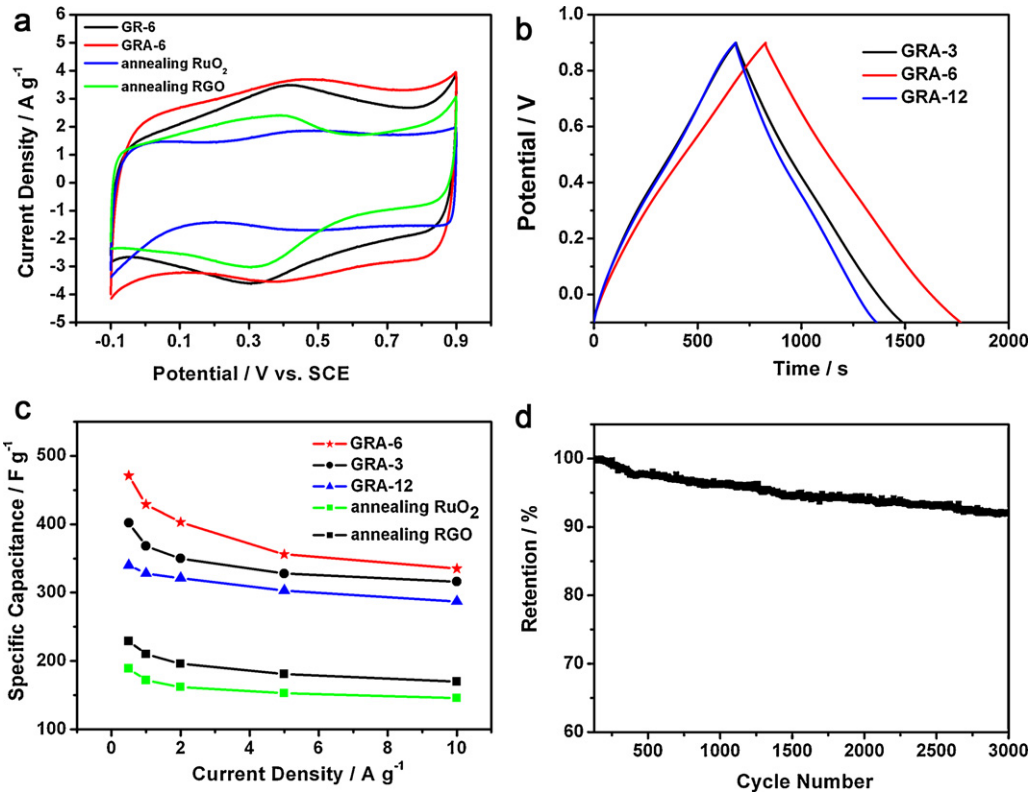

Fig. 7. (a) CV profiles of, GR-6, GRA-6 and RGO and RuO_2 after annealing at 10 mV s^{-1}, (b) Charge/discharge plots of GRA-3, GRA-6 and GRA-12 at 0.5 A g^{-1}, (c) specific capacitance of RGO and RuO_2 after annealing, GRA-3, GRA-6 and GRA-12 as a function of current densities and (d) cyclic performance of GRA-6 at 5 A g^{-1}.

due to condensation of hydroxyl of $Ru(OH)_4$ anchoring on reduced GO. With prolonging hydrothermal time, continuous reduction of oxygen in RGO sheets and gradual growth of RuO_2 occurs after depositing. Electron transfer of RuO_2 with high water content is limited for mere hydrothermal synthesis, it is essential to have the composites heated at a low temperature in air. Once through annealing at 150 °C, crystallization begins to arise for RuO_2 nanodots on RGO sheets. When RuO_2 nanodots are subjected to the same hydrothermal protocol without GO, condensation of hydroxyl and crystallization of RuO_2 occurs, which is evident from the sharp peaks of RuO_2 in the XRD pattern. The TEM and XRD results of pure RuO_2 are so much different from that of other hydrothermal synthesis [22] because of the tiny difference in the synthesis. When adding NaOH solution in our experiment, RuO_2 forms before the hydrothermal reaction. So the temperature, pressure and time are not desirable for pure RuO_2 because crystallization occurs even if at above 175 °C in an ambient environment [21]. But here it is necessary to inject NaOH solution so that it can prevent from agglomeration and restack of GO in $RuCl_3$ solution. Moreover, it seems that injecting NaOH solution does not decay the capacitance of the composites. From the XRD results, crystallization of the RuO_2 single phase is prevented in the presence of GO in the hydrothermal course, maybe because reduction of GO and co-precipitation occur before crystallization of RuO_2. In order to prove the homogeneity in the composites, element mapping images are obtained in all composites by EDS. Typically, the FESEM and element mapping images of GRA-6 are displayed in Fig. 6f and its inset. The contents of C, O and Ru are 33, 33 and 34 wt.%. Alternately, the content of RuO_2 is 45 wt.%, which is totally consistent to the TGA result. It is also observed that C, O and Ru element homogeneously and densely distributes in the random selected dashed frame.

The conductivity values of GRA-6 and RGO after annealing are 30 and 0.001 S cm^{-1}, respectively. Obviously, the relatively high conductivity of the composite owes to the high conductivity of RuO_2 whose conductivity reaches 300 S cm^{-1} [21].

In order to optimize the capacitive behaviours of the composites, the electrochemical properties of the samples with different parameters are compared. The CV profiles of GR-6, GRA-6 and RuO_2 and RGO after annealing measured at 10 mV s^{-1} are described in Fig. 7a. A featureless curve is observed for GRA-6 but a nonrectangular shape for GR-6, suggesting that the annealing material has a more ideal capacitive behaviour. The current response of GRA-6 is higher than that of GR-6 at both high and low potential regions. The improvement of 44 F g^{-1} for GRA-6 mainly originates from the formation of rutile-like RuO_2 chains in three dimensions [32], which promotes the electrical conductivity of the composites. On the contrary, pure RuO_2 after annealing shows poorer performance even than RGO after annealing, which is a result of decreasing in mean electron transfer number due to the undesirable hydrothermal treatments in such condition. So far, it can be concluded that only the capacitive nature of annealing composites is worth studying. As shown in Fig. 7b, the electrochemical properties of GRA-3, GRA-6 and GRA-12 are compared by the charge/discharge curves at the current density of 0.5 A g^{-1}. Remarkably, GRA-6 possesses a maximum specific capacitance of 471 F g^{-1} when only 45 wt% of RuO_2 is loaded, while the capacitance values of GRA-3 and GRA-12 are 402 and 340 F g^{-1}. As mentioned above, the hydrothermal and annealing treatments can render gradual growth and even crystallization of RuO_2, apart from reduction of oxygen on RGO sheets. As revealed by the previous work, RGO with relatively low oxygen content will show optimal electrochemical performance [11,33]. Yet crystallization leads to the formation of inactive bridging oxo bonds within RuO_2 with low water content. Although the original mesoporosity of RuO_2 nanodots is maintained by the hydrothermal method to favor the penetration of electrolytes into the electrode matrix, the increased inactive sites decrease the mean electron transfer number and the crystals with low water content still degrade the proton

diffusion. So the highest capacitance obtained with hydrothermal time of 6 h is a result of compromised effects between RGO and RuO_2 based on the two electrochemical mechanisms [34]. Note that the potential below point of zero charge could reverse the polarity of the electrode, the specific capacitance of RuO_2 after annealing is calculated in the range from 0 to 0.9 V. As shown in Fig. 7c, the highest capacitance of RuO_2 is only 189 F g^{-1} at 0.5 A g^{-1}, much lower than that in other reports [35–37]. Additionally, 229 F g^{-1} of the capacitance is obtained by RGO after annealing at the same condition. The sum capacitance of 45% of RuO_2 and 55% of RGO after annealing reaches only 211 F g^{-1}, much smaller than that of GRA-6, inferring that synergistic effects between RGO and RuO_2 contribute on the extra capacitance. Fig. 7c also presents the retention trend of GRA-3, GRA-6, GRA-12 and RuO_2 and RGO after annealing. When the capacitance at 0.5 A g^{-1} is a reference, the best retention of 84% at 10 A g^{-1} is viewed in GRA-12. The retention ratios of the other three samples are all above 71%, suggesting that good retention and capacitance can be obtained in GRA-6 simultaneously. The cycling durability of GRA-6 at 5 A g^{-1} is displayed in Fig. 7d. Its capacitive retention still reaches 92% of the max capacitance after 3000 cycles.

4. Conclusions

We firstly have employed GO as the precursor to synthesize RGO/RuO_2 composites by hydrothermal and annealing treatments. The usage of NaOH solution to adjust pH of GO colloids leads to homogeneous ruthenium oxide deposited on reduced graphene oxide sheets. EDS analysis describes the excellent distribution of Ru on RGO sheets. High degree of crystallization in RuO_2 is disclosed by XRD and the pure RuO_2 shows poor capacitance. Composites with 40 wt% RuO_2 exhibit good electrochemical properties. The optimal hydrothermal time of 6 h is established by comparing their capacitance. The best sample exhibits a maximum capacitance of 471 F g^{-1} at 0.5 A g^{-1}. Moreover, its rate capability is comparable to pure crystalline RuO_2 and its life-time retention is 92% even if after 3000 cycles. The outstanding integrative capacitive nature is attributed to the uniformity of RuO_2 on RGO and the synergistic effects between them.

Acknowledgements

This work was supported by the Knowledge Innovation Program of the Chinese Academy of Sciences (no. KJCX2-YW-W26), Beijing Municipal Science and Technology Commission (no. Z111100056011007), and the National Natural Science Foundation of China (no. 21001103 and 51025726).

References

[1] M. Gao, X. Chen, H. Pan, L. Xiang, F. Wu, Y. Liu, Electrochim. Acta 55 (2010) 9067–9074.
[2] M. Gao, Y. Lin, Y. Yin, Y. Liu, H. Pan, Electrochim. Acta 55 (2010) 8043–8050.
[3] P. Simon, Y. Gogotsi, Nat. Mater. 7 (2008) 845–854.
[4] K. Karthikeyan, V. Aravindan, S.B. Lee, I.C. Jang, H.H. Lim, G.J. Park, M. Yoshio, Y.S. Lee, J. Alloys Compd. 504 (2010) 224–227.
[5] R.R. Salunkhe, K. Jang, H. Yu, S. Yu, T. Ganesh, S.-H. Han, H. Ahn, J. Alloys Compd. 509 (2011) 6677–6682.
[6] D.P. Dubal, S.V. Patil, A.D. Jagadale, C.D. Lokhande, J. Alloys Compd. 509 (2011) 8183–8188.
[7] K.S. Novoselov, A.K. Geim, S.V. Morozov, D. Jiang, Y. Zhang, S.V. Dubonos, I.V. Grigorieva, A.A. Firsov, Science 306 (2004) 666–669.
[8] Y. Chen, X. Zhang, P. Yu, Y. Ma, Chem. Commun. 452 (2009) 7–4529.
[9] B. Wang, Y. Wang, J. Park, H. Ahn, G. Wang, J. Alloys Compd. 509 (2011) 7778–7783.
[10] Y. Chen, X. Zhang, P. Yu, Y. Ma, J. Power Sources 195 (2010) 3031–3035.
[11] Y. Chen, X. Zhang, D. Zhang, P. Yu, Y. Ma, Carbon 49 (2011) 573–580.
[12] S.R.C. Vivekchand, C.S. Rout, K.S. Subrahmanyam, A. Govindaraj, C.N.R. Rao, J. Chem. Sci. 120 (2008) 9–13.
[13] M.D. Stoller, S. Park, Y. Zhu, J. An, R.S. Ruoff, Nano Lett. 8 (2008) 3498–3502.
[14] D.A.C. Brownson, D.K. Kampouris, C.E. Banks, J. Power Sources 196 (2011) 4873–4885.
[15] J. Yan, T. Wei, B. Shao, F. Ma, Z. Fan, M. Zhang, C. Zheng, Y. Shang, W. Qian, F. Wei, Carbon 48 (2010) 1731–1737.
[16] C. Liu, K. Wang, S. Luo, Y. Tang, L. Chen, Small 7 (2011) 1203–1206.
[17] S.-Y. Yang, K.-H. Chang, Y.-F. Lee, C.-C.M. Ma, C.-C. Hu, Electrochem. Commun. 12 (2010) 1206–1209.
[18] Q. Wu, Y. Xu, Z. Yao, A. Liu, G. Shi, ACS Nano 4 (2010) 1963–1970.
[19] C.-C. Hu, W.-C. Chen, Electrochim. Acta 49 (2004) 3469–3477.
[20] U.M. Patil, S.B. Kulkarni, V.S. Jamadade, C.D. Lokhande, J. Alloys Compd. 509 (2011) 1677–1682.
[21] J.P. Zheng, P.J. Cygan, T.R. Jow, J. Electrochem. Soc. 142 (1995) 2699–2703.
[22] K.-H. Chang, C.-C. Hu, C.-Y. Chou, Chem. Mater. 19 (2007) 2112–2119.
[23] K.-H. Chang, C.-C. Hu, C.-Y. Chou, Electrochim. Acta 54 (2009) 978–983.
[24] Z.S. Wu, D.W. Wang, W. Ren, J. Zhao, G. Zhou, F. Li, H.M. Cheng, Adv. Funct. Mater. 20 (2010) 3595–3602.
[25] C. Nethravathi, M. Rajamathi, Carbon 46 (2008) 1994–1998.
[26] W.S. Hummers, R.E. Offeman, J. Am. Chem. Soc. 80 (1958) 1339.
[27] K.-H. Chang, Y.-F. Lee, C.-C. Hu, C.-I. Chang, C.-L. Liu, Y.-L. Yang, Chem. Commun. 46 (2010) 7957–7959.
[28] C.-C. Wang, C.-C. Hu, Carbon 43 (2005) 1926–1935.
[29] S.-Y. Yang, K.-H. Chang, H.-W. Tien, Y.-F. Lee, S.-M. Li, Y.-S. Wang, J.-Y. Wang, C.-C.M. Ma, C.-C. Hu, J. Mater. Chem. 21 (2011) 2374–2380.
[30] J.C. Groen, L.A.A. Peffer, J. Pérez-Ramírez, Microporous Mesoporous Mater. 60 (2003) 1–17.
[31] K.-H. Chang, C.-C. Hu, Appl. Phys. Lett. 88 (2006) 193102–193103.
[32] C.-C. Hu, W.-C. Chen, K.-H. Chang, J. Electrochem. Soc. 151 (2004) A281–A290.
[33] Z. Lin, Y. Liu, Y. Yao, O.J. Hildreth, Z. Li, K. Moon, C.-p. Wong, J. Phys. Chem. C 115 (2011) 7120–7125.
[34] Y. Wang, C.Y. Foo, T.K. Hoo, M. Ng, J. Lin, Chem. Eur. J. 16 (2010) 3598–3603.
[35] S.H. Oh, L.F. Nazar, J. Mater. Chem. 20 (2010) 3834–3839.
[36] R.-R. Bi, X.-L. Wu, F.-F. Cao, L.-Y. Jiang, Y.-G. Guo, L.-J. Wan, J. Phys. Chem. C 114 (2010) 2448–2451.
[37] C.-C. Hu, K.-H. Chang, M.-C. Lin, Y.-T. Wu, Nano Lett. 6 (2006) 2690–2695.